International Journal of Fluid Machinery and Systems
Vol. 3, No. 2, April-June 2010

Original Paper

Suppression of Cavitation Instabilities in an Inducer by Circumferential Groove and Explanation of Higher Frequency Components

Donghyuk Kang[1], Yusuke Arimoto[1], Koichi Yonezawa[1], Hironori Horiguchi[1], Yutaka Kawata[2], Chunill Hah[3] and Yoshinobu Tsujimoto[1]

[1]Graduate School of Engineering Science, Osaka University
1-3 Machikaneyama, Toyonaka, Osaka, 560-8531, Japan
[2]Faculty of Engineering, Osaka Institute of Technology,
5-16-1 Ohmiya, Asahi, Osaka, Osaka 535-8585, Japan
[3]NASA Glenn Research Center,
MS 5-11, Cleveland, Ohio 44135

Abstract

The purpose of the present research is to suppress cavitation instabilities by using a circumferential groove. The circumferential groove was designed based on CFD so that the tip leakage vortex is trapped by the groove and does not interact with the next blade. Experimental results show that the groove can suppress rotating cavitation, asymmetric cavitation and cavitation surge. However, weak instabilities with higher frequency could not be suppressed by the groove. From the analysis of pressure pattern similar to that for rotor-stator interaction, it was found that the higher frequency components are caused by the interaction of backflow vortices with the inducer blades.

Keywords: Inducer, Cavitation instabilities, Circumferential groove, Higher frequency component

1. Introduction

The suppression of cavitation instability is one of the most important issues for the design of reliable turbo-pump inducers for rocket engines. Until now, various cavitation instabilities have been identified [1], including cavitation surge, rotating cavitation, and their higher order modes. They may cause high dynamic loads on the shaft and the blades, and threaten the reliability of the engine.

In parallel with the theoretical and numerical researches [2~6] to clarify the characteristics of cavitation instabilities, various experimental studies for the suppression of cavitation instabilities were made. Kamijo et al. [7] have used enlarged casings, Kim et al.[8] have installed asymmetric obstacle plates in the suction pipe. Although these methods were effective for the suppression of particular cavitation instability, cavitation instabilities were not suppressed completely and the suppression mechanism was not clear.

By using axial grooves on the casing, Shimiya et al [9] have found experimentally that cavitation instabilities can be avoided by avoiding the interaction of tip cavities with the leading edge of the next blade. Recently, authors have found that there exists a disturbance flow toward the trailing edge of tip cavity. It reduces the incidence angle to the next blade and causes cavitation instabilities [10]. This also suggests that cavitation instabilities can be suppressed by avoiding the interaction of the tip cavity with the leading edge of next blade. Based on this design guideline, three inducers were designed to avoid cavitation instabilities and they stably operated without cavitation instabilities [11].

For a transonic axial compressor, it was shown [12] that the stall margin can be improved by controlling the tip leakage vortex by using circumferential grooves. The purpose of present research is to suppress cavitation instabilities by using a circumferential groove. The circumferential groove was designed using a CFD so that the groove can trap tip cavities and avoid the interaction with the next blade. It was found that the groove can suppress rotating cavitation, attached cavitation and cavitation surge. However, weak higher frequency components could not be suppressed by the groove. From the analysis of pressure pattern similar to that for rotor-stator interaction, it was found that the higher frequency components are caused by the interaction of backflow vortices with the inducer blades.

Received February 23 2010; accepted for publication June 1 2010: Review conducted by Prof. Zhang Yangjun. (Paper number O10003S)
Corresponding author: Yoshinobu Tsujimoto, Professor, tujimoto@me.es.osaka-u.ac.jp

This paper will be presented at the 25th IAHR Symposium on Hydraulic Machinery and Systems, September 20-24, 2010, Romania.

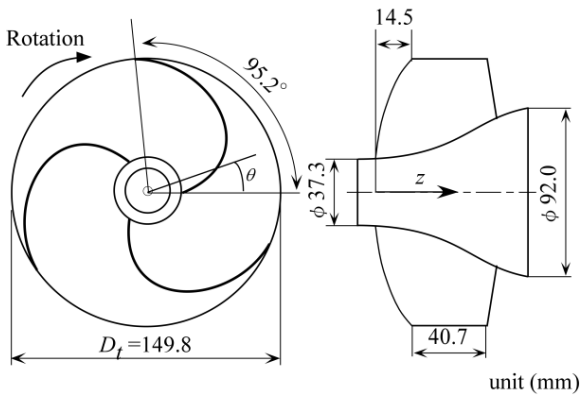

Fig. 1 Geometry of inducer

Table 1 Main specifications of inducer

Number of blades	3
Tip diameter (mm), D_t	149.8
Tip clearance (mm)	0.5
Sweep angle (deg)	95.2
Inlet tip blade angle (deg)	7.5
Outlet tip blade angle (deg)	9.0
Hub / Tip ratio at inlet	0.25
Hub / Tip ratio at outlet	0.51
Solidity at tip	1.91
Design flow coefficient, ϕ_d	0.078

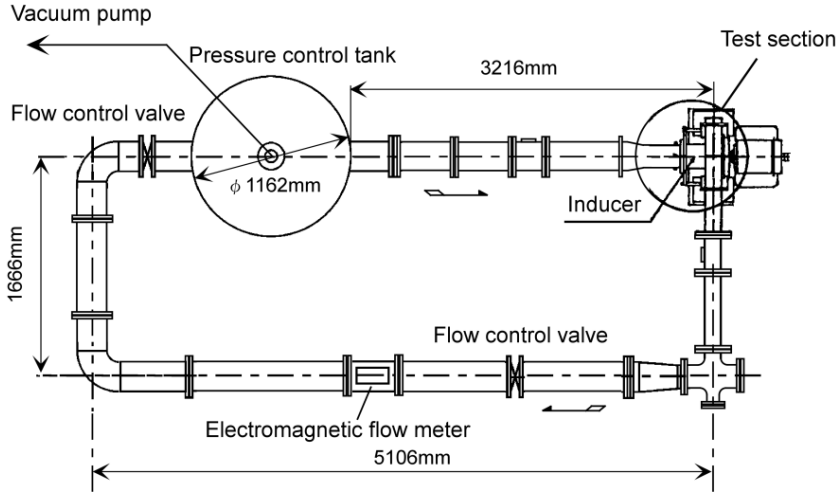

Fig. 2 Test facility

2. Experimental and Computational Methods

2.1 Experimental Method

Figure 1 and Table 1 show the leading edge geometry and geometrical properties of the inducer tested. The inducer has three blades with backward swept leading edge with the diameter of 149.8mm. The leading edge sweep angle is 95.2°, as shown in Fig.1. At the blade tip, the inlet and outlet blade angles are 7.5° and 9.0°, respectively. The blade angle $\beta(r)$ is determined by the helical condition of $r\times\tan\beta(r)=R_t\times\tan\beta_t$, where r is the radius, R_t is the radius of the impeller, and β_t is the blade angle at the tip. The design flow coefficient ϕ_d of the original inducer is 0.078. The flow coefficient ϕ is defined as v_1/U_t, where v_1 is the mean axial velocity in the plane at $z/D_t=0$, and U_t is the tip speed of the inducer.

Figure 2 shows the test facility. It is a closed type cavitation tunnel. The inlet pressure was adjusted by controlling the tank pressure with a vacuum pump. The flow rate ϕ was controlled by the butterfly valve located downstream of the impeller. The impeller is driven by an inverter motor. The working fluid is water at room temperature.

Figure 3 shows the details of the test section around the inducer with a straight casing. For the evaluation of static pressure coefficient ψ_s defined as $(p_2\text{-}p_1)/(\rho U_t^2)$, the inlet and outlet static pressures, p_1 and p_2, were measured at the locations 302mm upstream and 66mm downstream of the blade leading edge at the tip, respectively. For the examination of cavity oscillation, the inlet pressure fluctuations, p_a and p_b, were measured by pressure transducers flush mounted at the location 44mm upstream of the blade leading edge at the tip. The transducers are installed with circumferential interval of 90° to identify the mode of instabilities. The axial coordinate z is set in the downstream direction from the origin ($z/D_t=0$) at the leading edge of blades at root shown in Fig.1.

During the operation of the pump, the flow rate, the static pressures at the inlet and outlet of the impeller, the fluctuating pressure at the inlet, the water temperature and the rotational speed of impeller are transferred to a computer through an A/D converter. The casing was made of transparent acrylic resin for visual observation. Pictures were taken by a high-speed camera with the frame rate of 4500 frame/sec.

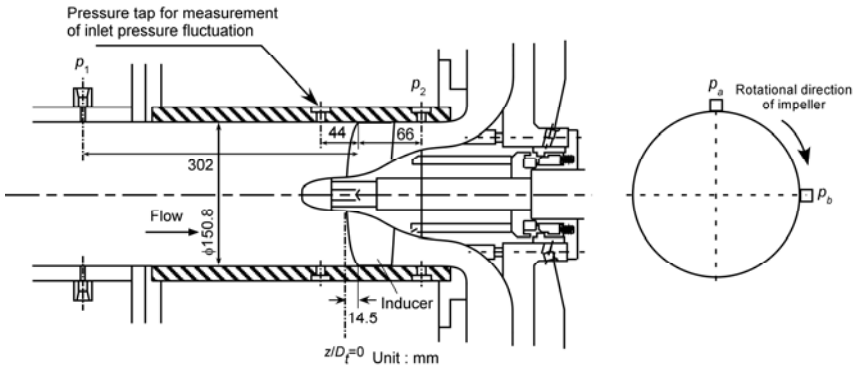

Fig. 3 Test section

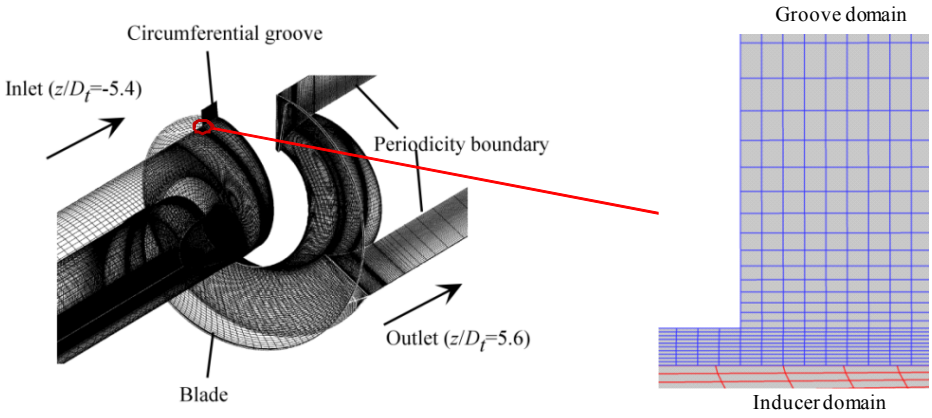

(a) One blade channel for steady calculations

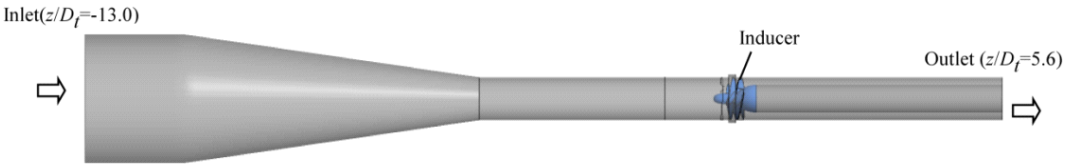

(b) All blade channels for the unsteady calculation

Fig. 4 Computational domains for steady and unsteady calculations

2.2 Computational Method

A commercial software, ANSYS-CFX11.0, was used for the simulation of the cavitating flow through the inducer. Three-dimensional Reynolds averaged Navier-Stokes (RANS) equations were solved by finite volume method with hybrid unstructured grids. The k-ω turbulence model was used. The cavitation model is based on the homogenous multiphase flow framework of the CFD solver taking into account the dynamics of cavitation bubbles by solving a simplified Reyleigh-Plesset equation [13]. The effect of cavitation is taken into account by adding a special source term into the continuity equation. The working fluids were water and its vapor. The total pressure and no circumferential velocity were specified at the inlet and the mass flow rate was specified at the outlet. The rotational speed was fixed at 3000rpm, which is the same as the experiment. The groove and inducer meshes with non-matching interfaces were used as shown in Fig.4(a) and the continuities of mass and momentum are assumed at the interface. The mesh in the tip gap is also non-matching with radial meshes.

For the steady calculations, the flow in one blade channel was calculated by assuming the circumferential periodicity as shown in Fig.4.(a). The number of cells in the inducer is about 2,200,000 and about 150.000 in the groove. The lengths of inlet and outlet pipes are 5.4 and 5.6 times the diameter of impeller, respectively. The result of noncavitating flow was used as the initial value for the simulation of cavitating flow. For the unsteady calculation, all blade channels of the inducer were calculated as shown in Fig.4(b). The time step is 1/400 of a revolution of the impeller and the second order schemes in space and time were used. The number of computational cells of all blade channels is 3,800,000. The lengths of inlet and outlet pipes are 13.0 and 5.6 times the diameter of impeller, respectively. To obtain stable solution, the inlet pipe was enlarged as shown in Fig.4(b). The result of steady calculation was used as the initial value for the simulation of unsteady cavitating flow.

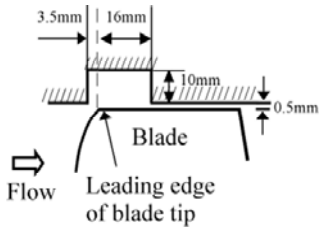

Fig. 5 Geometry of circumferential grooves

Table 2 Static pressure coefficient at ϕ/ϕ_d=1.0

	Straight casing	Grooved casing
$\eta(\sigma=\infty)$	0.784	0.763
ψ_s $(\sigma=\infty)$	0.1263	0.1213
$\psi_s(\sigma=0.10)$	0.1256	0.1190
$\psi_s(\sigma=0.04)$	0.1267	0.1214

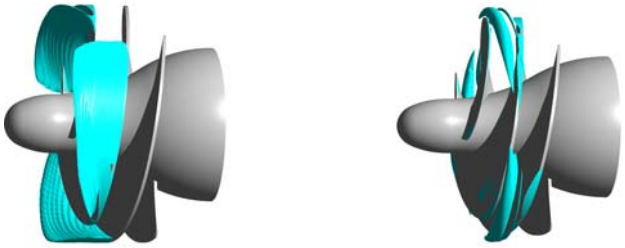

(a) Straight casing **(b)** Grooved casing

Fig. 6 Comparison of cavity geometry at ϕ/ϕ_d=1.0, σ=0.04 and α=0.01

3. Computational Results

3.1 Design of Circumferential Grooves

The design concept of circumferential groove is to trap the tip leakage vortex in a circumferential groove, which would be helpful to avoid the interaction of tip cavities with the leading edge of next blade. Firstly, we numerically investigated the effect of groove geometries on the tip leakage vortex and found the optimum geometries to "pack" the tip leakage vortex in the circumferential groove.

Figure 5 shows the geometry of circumferential groove tested. The width of groove is 19.5mm and the upstream edge is located 3.5mm upstream of the leading edge of blade tip. The depth of groove is 10mm for the impeller with diameter 149.8mm.

Table 2 shows the hydraulic efficiency η and static pressure coefficient ψ_s obtained from the calculation. The hydraulic efficiency was evaluated from

$$\eta = \frac{P_o}{P_i} = \frac{\int \rho \cdot v_z \cdot (\frac{p}{\rho} + \frac{1}{2} \cdot v^2) ds_2 - \int \rho \cdot v_z \cdot (\frac{p}{\rho} + \frac{1}{2} \cdot v^2) ds_1}{\int \rho \cdot v_z \cdot (r \cdot \omega \cdot v_\theta) ds_2 - \int \rho \cdot v_z \cdot (r \cdot \omega \cdot v_\theta) ds_1} \tag{1}$$

where, v is the absolute velocity, v_θ is the absolute circumferential velocity, ω is the angular velocity and the suffix numbers of 1 and 2 show the inlet and outlet. With the grooved casing, the pressure coefficient and hydraulic efficiency are slightly lower than that with the straight casing.

3.2 Flow Characteristic

Figure 6 shows the cavity geometries at σ=0.04. The cavitation number σ is defined as $(p_1\text{-}p_v)/(\rho U_t^2/2)$ where p_v is the vapor pressure and p_1 is the inlet pressure at the location shown in Fig.3. The cavity is shown by the isovalue surface with the void fraction α=0.01. With the grooved casing, the cavity volume is remarkably reduced as compared with the straight casing and the separating point of tip leakage vortex cavity is moved downstream.

To clarify the effect of cavity, the velocity disturbance caused by the cavity was evaluated by subtracting the velocity of non-cavitating flow from that of cavitating flow. The disturbance velocity vectors and void fraction distributions in z-θ and r-z planes are shown in Fig.7. With the straight casing, the disturbance flow near the cavity trailing edge has an axial component which reduces the incidence angle to the next blade. It has been shown that the axial disturbance flow causes alternate blade cavitation, cavitation surge and rotating cavitation [10]. With the grooved casing, the disturbance flow is weaker and no positive axial flow is found near the leading edge of the blade. This is preferable to suppress cavitation instabilities.

Figures 8 and 9 show the velocity vectors and void fraction distributions at ϕ/ϕ_d=1.0 and σ=0.04 in r-z planes. With the straight casing, the tip leakage vortex core appears near the leading edge at blade tip shown in Fig.8(a), and then it extends upstream as θ is increased. The cavity appears not in the tip leakage vortex but in the lower pressure region around the junction of blade suction surface and the casing.

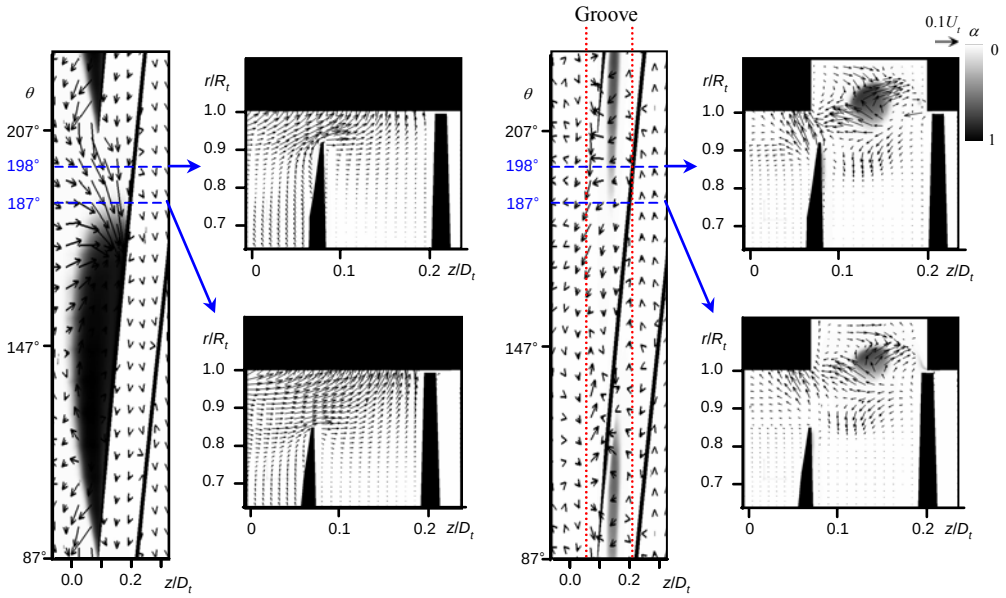

(a) Straight casing **(b)** Grooved casing

Fig. 7 Disturbance velocity vector and void fraction distribution at r/R_t=0.98, ϕ/ϕ_d=1.0 and σ=0.04

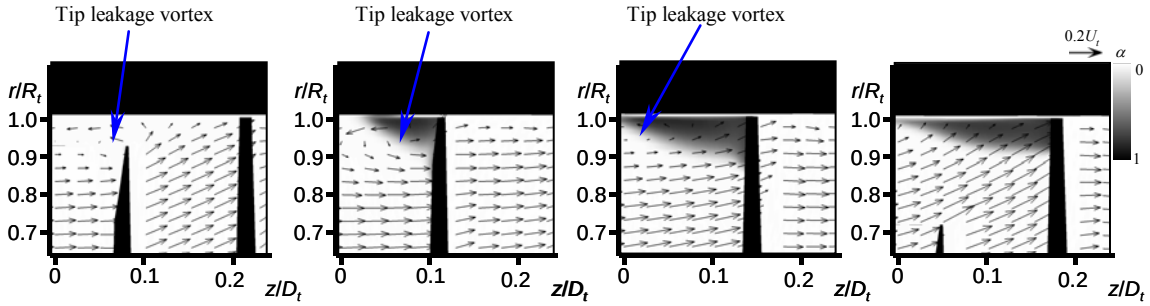

(a) θ= 80° **(b)** θ=110° **(c)** θ=140° **(d)** θ=170°

Fig. 8 Velocity vector and void fraction distribution in meridional planes with the straight casing at ϕ/ϕ_d=1.0 and σ=0.04

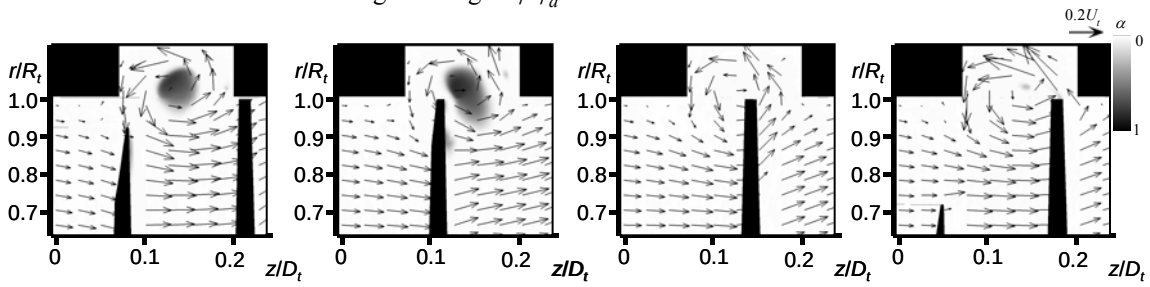

(a) θ= 80° **(b)** θ=110° **(c)** θ=140° **(d)** θ=170°

Fig. 9 The same as for Fig.8 with the grooved casing

With the grooved casing, the tip leakage vortex cavity develops only in the circumferential groove. The vortex is enhanced by the jet at θ=170° from the clearance between the pressure surface of the blade and the rear wall of the groove. At θ=110°, a weak cavity is observed on the pressure surface. This is caused by the interaction with the tip leakage vortex cavity. However, the head ψ_s= 0.1214 at σ=0.04 is not significantly lower than the head ψ_s= 0.1213 under noncavitating condition. Inward radial velocity is observed in the upstream edge of the circumferential groove, suppressing the tip leakage vortex cavity on the suction side of blade tip.

Figure 10 shows the blade pressure distributions at r/R_t=0.98. At σ=0.10, a cavity appears on the suction surface in 90°<θ <135° with the straight casing but no cavity is found with the grooved casing. With the grooved casing, negative blade loading is found near the leading edge and the blade loading is moved downstream. Thus, we can control the blade loading by the groove. At σ=0.04, the cavitating region is extended to 90°<θ <175° with the straight casing. With the grooved casing, the effect of cavitation number is smaller although a cavity appears in 100°<θ<120° on the pressure surface. Figure 9 shows that the cavity is caused by the interaction with the tip leakage vortex cavity of the preceding blade.

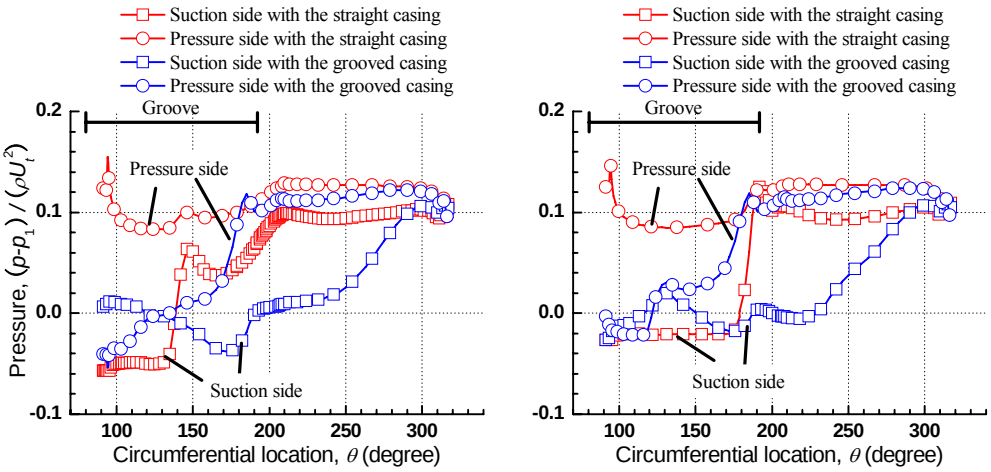

(a) σ=0.1 **(b)** σ=0.04

Fig. 10 Pressure distribution at r/R_t=0.98, ϕ/ϕ_d=1.0

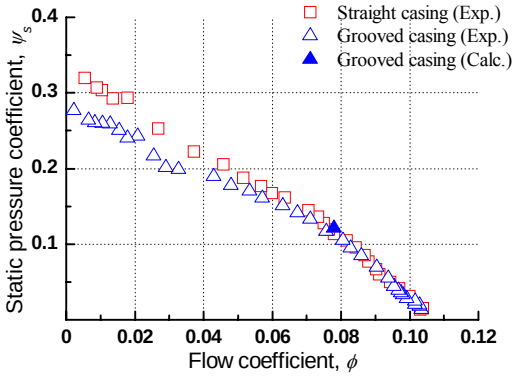

Fig. 11 Noncavitating performance curves at1500rpm

4. Experimental Results

4.1 Non-Cavitating Performance

Figure 11 shows the non-cavitating performance curves obtained from the experiments and the computation. With the grooved casing, the static pressure coefficients at lower flow coefficients are lower than that with the straight casing. However, the decrease of static pressure coefficient is acceptable at the design flow coefficient, ϕ=0.078.

4.2 Suction Performance

Figure 12 compares the suction performance curve with and without the groove. With the straight casing [14], the test was conducted at 3000rpm with orifice plates at the inlet, while the test was conducted at 4500rpm without the orifice plates for the case with the grooved casing. The larger scatter with the straight casing is caused by cavitation instabilities with some effects of bubbles from the orifice plates. We find that the suction performance is somewhat improved by the groove.

4.3 Cavitation Instabilities

Figures 13~15 show the spectra of inlet pressure fluctuations measured by the pressure transducers flush mounted 44mm upstream of the blade leading edge at the tip. The horizontal axis shows the frequency, the vertical axis shows the magnitude of the pressure fluctuation $\Delta\psi$ defined as $\Delta p/(\rho U_t^2)$ and the depth axis shows the cavitation number σ. N is the frequency 50Hz of the impeller rotation. The phase difference of pressure fluctuations measured at two circumferential locations 90 ° apart are shown for typical components. The negative/positive phase difference means that the pressure pattern rotates in the same/opposite direction of the impeller rotation.

In 0<f<150Hz, with the circumferential groove, rotating cavitation, cavitation surge and asymmetric cavitation were successfully suppressed at all flow rates except for weak instabilities observed at ϕ/ϕ_d= 1.1.

In 150< f<500Hz, instabilities with higher frequency components are observed. A higher frequency component with 4.8N was observed in the engine firing tests and water tests on liquid hydrogen turbopump inducer for HII rocket [15]. In this case, the phase difference was 0°. The higher frequency components are important since they can be closer to the natural frequencies of blade bending mode. For this reason, extensive studies have been made to avoid the higher frequency components [16]. In the present tests, we find components around 5N, 7~8N, and 10N.The phase difference is different from case to case but can be assorted into groups around zero (surge mode), -90°(one cell rotating forward) and +90°(one cell rotating backward). The cause of these higher frequency modes is discussed later.

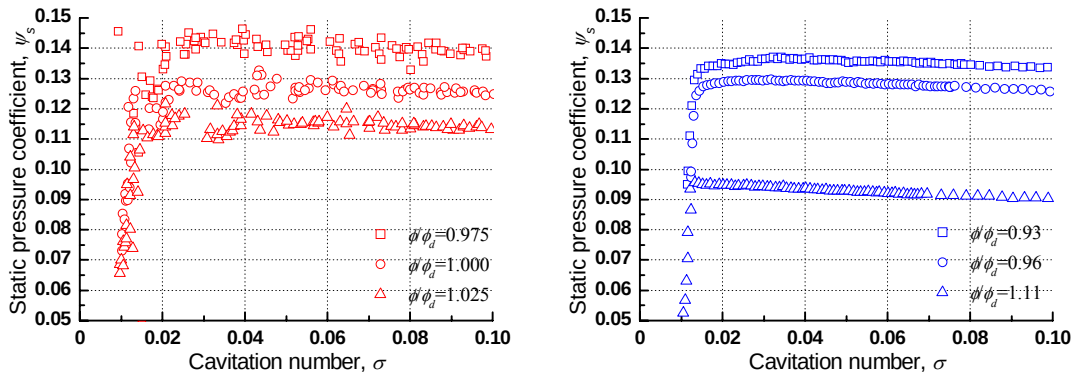

(a) Straight casing **(b)** Grooved casing

Fig. 12 Comparison of suction performance curves

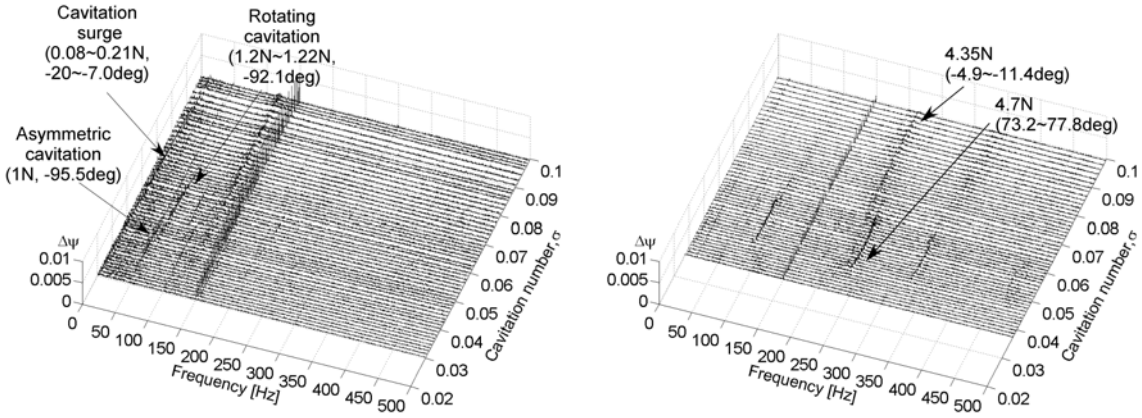

(a) Straight casing **(b)** Grooved casing

Fig.13 Spectra of inlet pressure oscillation at ϕ/ϕ_d=0.9

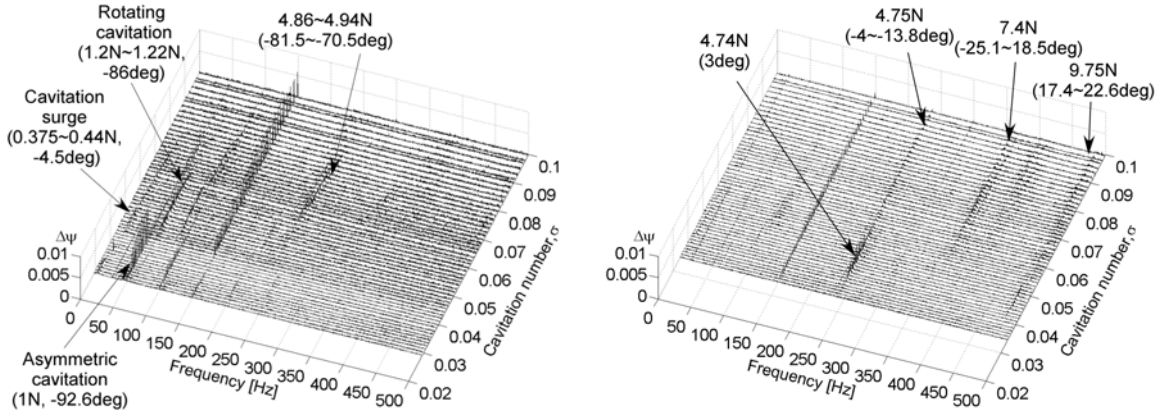

(a) Straight casing **(b)** Grooved casing

Fig.14 Spectra of inlet pressure oscillation at ϕ/ϕ_d=1.0

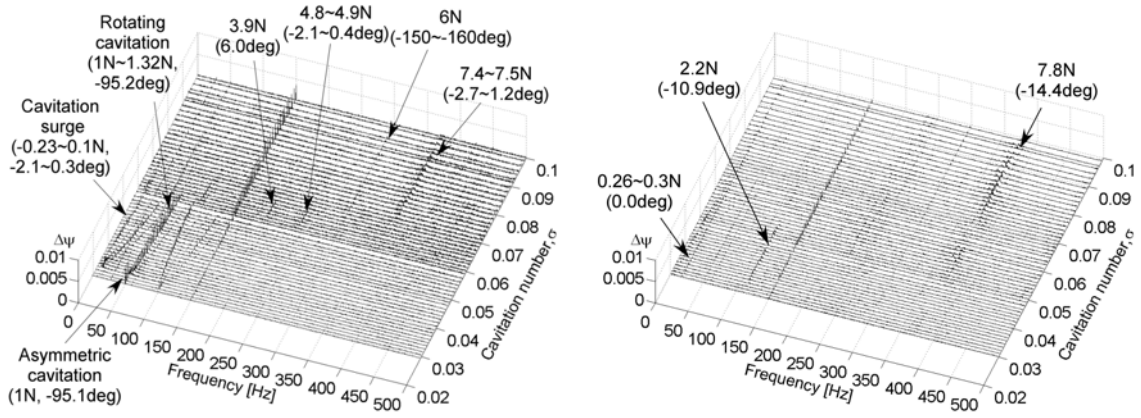

(a) Straight casing **(b)** Grooved casing

Fig.15 Spectra of inlet pressure oscillation at ϕ/ϕ_d=1.1

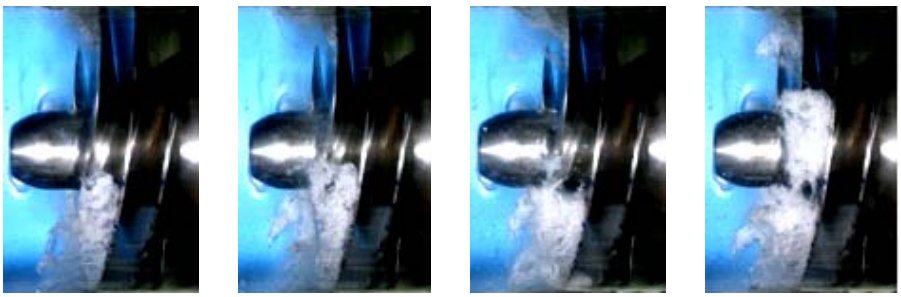

(a) = 0.10 **(b)** = 0.08 **(c)** = 0.06 (Shorter cavity) **(d)** = 0.06 (Longer cavity)

Fig.16 Cavity geometries with the straight casing at / $_d$=1.0

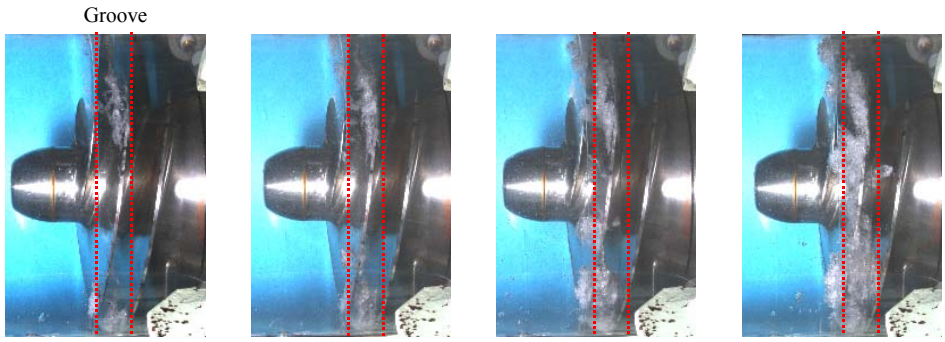

(a) σ= 0.1 **(b)** σ= 0.08 **(c)** σ= 0.06 **(d)** σ= 0.04

Fig.17 Cavity geometries with the grooved casing at ϕ/ϕ_d=1.0

4.4 Cavity Geometry

Figures 16 and 17 compare the pictures of cavities at the design flow coefficient at ϕ/ϕ_d=1.0 with and without the groove. We observe the following differences.

(1) With the straight casing, the cavity occupies the entire tip region while the cavity mostly occurs in the groove with the grooved casing. This agrees with the numerical results shown in Figs.8 and 9.
(2) With the straight casing, the backflow vortex cavitation extends more upstream than the case with the groove. With the grooved casing, the backflow vortex cavitation extends only slightly from the upstream edge of the groove.

Although not shown, it was found that the increase of cavity volume with the decrease of flow rate was much smaller with the grooved casing. These results explain the reason why the cavitation instabilities were suppressed in a wide range of flow rate.

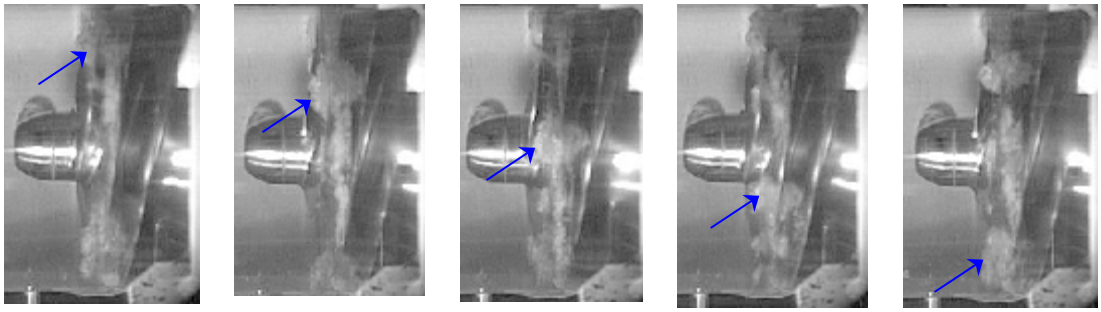

(a) 0 s **(b)** 0.0088s **(c)** 0.0177s **(d)** 0.0267s **(e)** 0.0355s

Fig.18 Propagation of backflow vortex cavities, from high-speed video at ϕ/ϕ_d=1.0 and σ=0.045

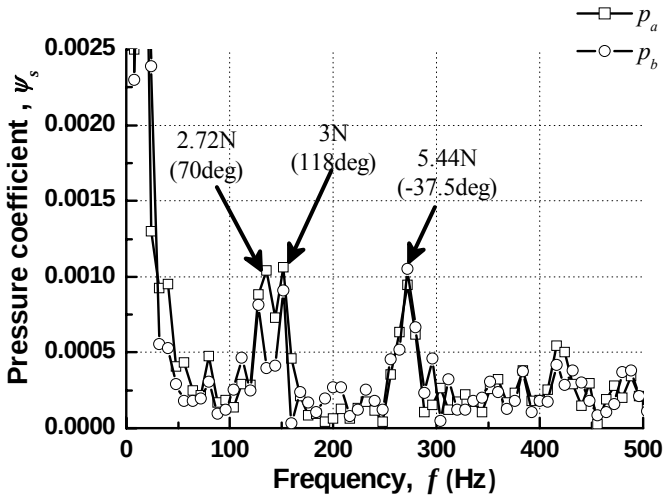

Fig.19 Spectrum of inlet pressure oscillation at ϕ/ϕ_d=0.9 and σ=0.050

4.5 Propagation of Backflow Vortex Cavity

Figure 18 shows the pictures of cavities from high-speed video to examine the propagation of backflow vortex cavities for the case with the grooved casing, at ϕ/ϕ_d=1.0 and σ=0.045. The propagation speed Ω_v is measured from the pictures and number of vortices N_v was evaluated by counting the passage of vortices. The results are shown in Table.3 where Ω_n is the impeller speed.

For the case without groove, the backflow vortex structure has been studied extensively [17] and it was found that the vortex structure is caused by the roll-up of the shear layer between the straight main flow and swirling backflow. It was found that the number of vortices is determined from the stability of vortices and the number decreases with the decrease of flow rates caused by the inward shift of the radial location of the vortices. It was also found that both the velocity and the number of vortices fluctuate largely with time. So, the values in Table 3 are only representative values.

Table 3 Propagation speed and number of vortices

ϕ/ϕ_d	σ	Ω_v	N_v
0.9 (Grooved casing)	0.055	$0.16\Omega_n$	7.99
1.0 (Grooved casing)	0.045	$0.13\Omega_n$	8.84
1.0 (Grooved casing)	0.080	$0.15\Omega_n$	10.7
1.1 (Grooved casing)	0.080	$0.11\Omega_n$	16.4
1.0 (Straight casing)	0.050	$0.12\Omega_n$	8~16

5. Cause of Higher Frequency Oscillations

5.1 Unsteady Calculation

To confirm the suppression of rotating cavitation and to clarify the cause of higher frequency components, unsteady calculation was made on full passage with the grooved casing, at ϕ/ϕ_d=0.9 and σ=0.05. The full passage calculation is needed to simulate rotating cavitation and backflow vortices.

Figure 19 shows the spectrum of inlet pressure fluctuation at the same location with the experiments. As expected, we do not have significant component around N=50Hz, suggesting that the rotating cavitation has been suppressed. In addition to the blade passing component and its modulations around $3N$=150Hz, we observe a component with $5.44N$.

Figure 20 shows the 3-D representation of iso-pressure surface of $\psi_c=(p-p_v)/(\rho U_t^2)$=0.083 and the pressure distributions in the plane of r/R_t=0.87 and at z/D_t=-0.2. We observe five vortices interacting with the blades. It was found that the vortices rotate at an absolute speed of 0.112 Ω_n Then, the vortex passage frequency observed on a blade is $5\times(1\text{-}0.112)\ \Omega_n$.=4.44 Ω_n. This is different from the frequency 5.44N found in the upstream pressure fluctuation.

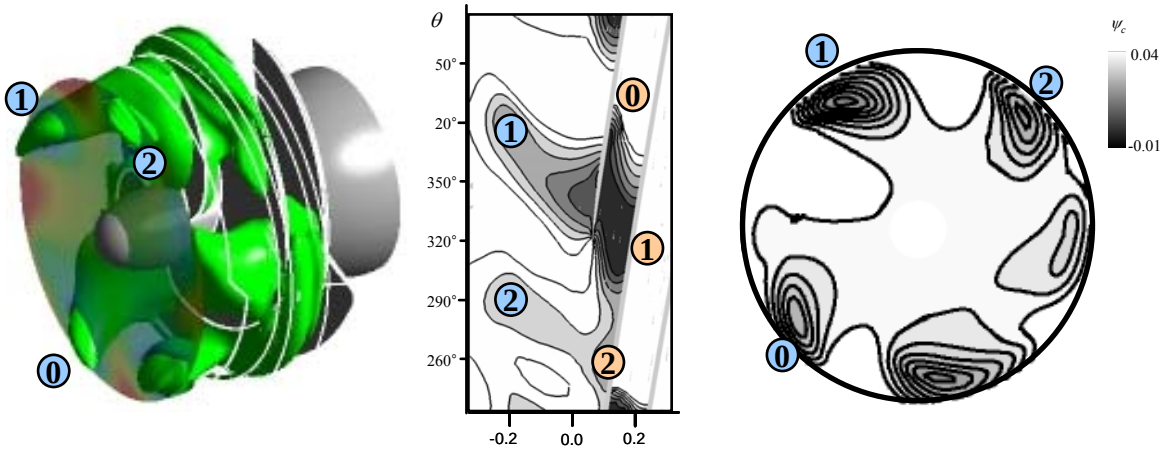

(a) Iso-pressure surface with ψ_c=0.083 **(b)** Pressure distribution in the plane of r/R_t=0.86 **(c)** Pressure distribution at z/D_t=-0.2

Fig.20 3-D representation of iso-pressure surface and the pressure distribution in the planes of r/R_t=0.86 and at z/D_t=-0.2 (ϕ/ϕ_d=0.9 and σ=0.050)

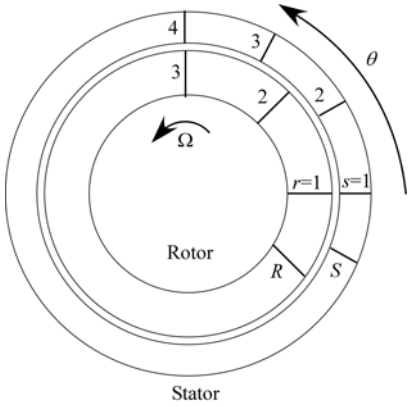

Fig.21 Rotor-stator interaction model

5.2 Rotating Modes due to Interaction

It is known that rotating modes occur due to rotor-stator interaction [18]. We first consider a rotor with R blades (r=1,…R) rotating with an angular speed of Ω and a stator with S blades (s=1,….S) as shown in Fig.21. We represent the pressure component caused by the interaction of a stator blade s=1 with R rotor blades (r=1,…R) by

$$p_{m,n}^{\ s=1}(\theta,t) = a_{m,n} \cdot \cos(m\theta - nR\Omega t)\,, \tag{2}$$

where m and n are the number of order in θ and t. Then the pressure pattern caused by the interaction of a stator blade s=q with R rotor blades (r=1,…R) can be represented by

$$p_{m,n}^{\ s=q}(\theta,t) = a_{m,n} \cdot \cos[m(\theta - \frac{2\pi}{S}(q-1)) - nR\Omega(t - \frac{2\pi}{S\Omega}(q-1))] \tag{3}$$

By adding up the effects of all stator blades (q=1~S), we obtain

$$\begin{aligned} p_{m,n}(\theta,t) &= a_{m,n} \cdot \sum_{q=1}^{S} \cos[m\theta - nR\Omega t - (m - nR)\frac{2\pi}{S}(q-1)] \\ &= \begin{cases} S \cdot a_{m,n} \cdot \cos(m\theta - nR\Omega t) & m = nR + kS \\ 0 & m \neq nR + kS \end{cases} \end{aligned} \tag{4}$$

where k is an arbitrary integer.

We consider the case when the "stator" is also rotating and represent the stator speed by Ω_v and the rotor speed by Ω_n. We introduce an absolute circumferential coordinate $\theta^* = \theta + \Omega_v t$. By putting $\theta = \theta^* - \Omega_v t$ and $\Omega = \Omega_n - \Omega_v$, we obtain

$$p_{m,n}(\theta^*,t) = S \cdot a_{m,n} \cdot \cos[m\theta^* - \{nR(\Omega_n - \Omega_v) + m\Omega_v\}t] \tag{5}$$

for the case with $m=nR+kS$.

Now we examine the pressure pattern caused by the interaction of N_v inlet backflow vortices with the impeller blades. We replace the number of stator blades S with the number of vortices N_v.

Table 4 shows possible cases of

$$m=nR+kN_v \tag{6}$$

for the case of R=3 and the frequency

$$\omega = nR(\Omega_n - \Omega_v) + m\Omega_v \tag{7}$$

obtained by assuming $\Omega_v/\Omega_n = 0.15$.

Table 4 Mode analysis with $k=-1$, R=3 and $\Omega_v=0.15\Omega_n$

	$m=nR+kN_v$ (n=2, N_v=5,6,7)	$m=nR+kN_v$ (n=3, N_v=8,9,10)	$m=nR+kN_v$ (n=4, N_v=11,12,13)
m=1	$1=2\times3-1\times5$, $\omega=5.25\Omega_n$	$1=3\times3-1\times8$, $\omega=7.8\Omega_n$	$1=4\times3-1\times11$, $\omega=10.35\Omega_n$
m=0	$0=2\times3-1\times6$, $\omega=5.1\Omega_n$	$0=3\times3-1\times9$, $\omega=7.65\Omega_n$	$0=4\times3-1\times12$, $\omega=10.2\Omega_n$
$m=-1$	$-1=2\times3-1\times7$, $\omega=4.95\Omega_n$	$-1=3\times3-1\times10$, $\omega=7.5\Omega_n$	$-1=4\times3-1\times13$, $\omega=10.05\Omega_n$

We find

(1) The circumferential mode number m changes easily with the change of vortex number N_v.
(2) The frequency is nearly constant in the groups of N_v=(5,6,7), N_v=(8,9,10), N_v=(11,12,13) and changes largely between N_v =7 and 8 or 10 and 11.

This corresponds to the experimental observations that

(1) Various modes occur with nearly the same frequency.
(2) The frequencies are around $5\Omega_n$, $7\Omega_n$, and $10\Omega_n$.

Table 5 compares the components observed in the experiments and the frequency of possible modes obtained by Eq.(7). Experimental values are used for Ω_v. Although not perfect, general agreement is obtained. This suggests that the higher frequency components are caused by the interaction of the backflow vortices with the blades. The discrepancy might be caused by the unsteady nature of the backflow vortices; the number of vortices and the propagation velocity changes irregularly with time.

Table 5 Comparison of the experimental and CFD results with the analysis

	Experiment, CFD					Analysis			
ϕ/ϕ_d	σ	N_v	ω	Ω_v	Phase delay (degree)	m	n	N_v	ω
0.9 (Groove, Exp.)	0.055	7.99	$4.7\Omega_n$	$0.16\Omega_n$	73.2~77.8	−1	2	7	$4.88\Omega_n$
1.0 (Groove, Exp.)	0.045	8.84	$4.74\Omega_n$	$0.13\Omega_n$	3	0	2	6	$5.22\Omega_n$
1.0 (Groove, Exp.)	0.080	10.7	$4.75\Omega_n$, $7.4\Omega_n$, $9.75\Omega_n$	$0.15\Omega_n$	-4~13.8, -25.1~18.5, 17.4~22.6	0 0 0	2 3 4	6 9 12	$5.1\Omega_n$ $7.65\Omega_n$ $10.2\Omega_n$
1.1 (Groove, Exp.)	0.080	16.4	$7.8\Omega_n$	$0.11\Omega_n$	-14.4	0	3	9	$8.01\Omega_n$
1.0 (Straight casing, Exp.)	0.080	8~16	$4.86\sim4.94\Omega_n$	$0.12\Omega_n$	-81.5~-70.5	1	2	5	$5.40\Omega_n$
0.9 (Groove, CFD)	0.050	5	$5.44\Omega_n$	$0.112\Omega_n$	-37.5	1	2	5	$5.44\Omega_n$

Figure 22 shows the spectra of pressure fluctuation in a 4-bladed inducer measured at $0.03D_t$ axial distance downstream from the blade leading edge at the tip [16]. We have a case of $0=2\times4-1\times8$ for $m=nR+kN_v$. For this case, the estimated frequency with $\Omega_v=0.15\Omega_n$ is $\omega=2\times4\times(1-0.15)\ \Omega_n=6.8\Omega_n$. Another case is $0=3\times4-1\times12$ with the frequency $\omega=3\times4\times(1-0.15)\ \Omega_n=10.2\Omega_n$. The frequencies are 4/3 times the frequencies for the 3-bladed inducer shown in Table 4. Figure 22 includes the components close to these frequencies.

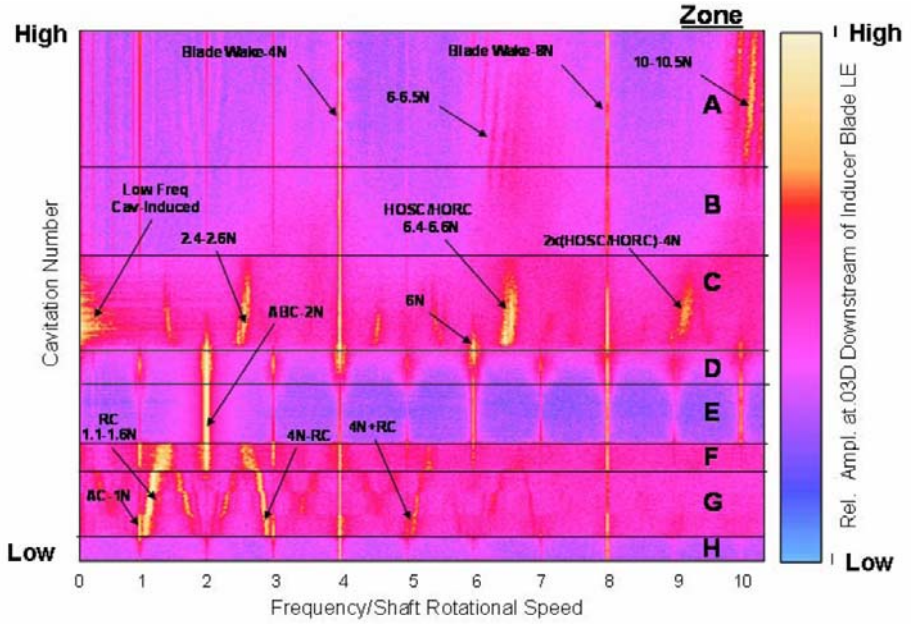

Fig.22 Spectra of pressure fluctuation in a 4-bladed inducer, from Subbaraman et al. [16]

6. Conclusions

The main findings of the present study are (1) that rotating cavitation and cavitation surge can be suppressed by the circumferential groove and (2) that the higher frequency components often observed before can be explained by the interaction of backflow vortices with the blades.

It was shown by flow visualization and CFD that the tip leakage vortex can be successfully trapped by the groove. CFD shows that the blade loading was moved downstream by the groove. Unfortunately, the higher frequency components could not be suppressed by the groove. Three dimensional unsteady CFD with cavitation suggested that the higher frequency components are caused by the interaction of backflow vortices with the blades. This was confirmed by the examination of the experimental results as compared with an interaction model similar to that for rotor-stator interaction proposed by Tyler & Sofrin. The model can explain the frequency and the mode of higher order frequency components.

The results of the present study suggest that higher frequency components can be avoided by avoiding backflow vortices by reducing the blade loading near the leading edge. However, the results with the groove with reduced leading edge loading have stronger higher frequency components. This suggests that further studies are needed to correlate the strength of backflow vortices and the strength of higher frequency components.

Acknowledgement

The experiments were carried out with the help of Mr.Jun Aono. The authors would like to thank also Mr.Sen Meng of PWR and Dr.Maria Subbaraman of Aerojet Corp. for their useful suggestions. This study was made under the support of Grant-in-Aid for Scientific Research (B).

Nomenclature

D_t	Diameter of inducer [m]	α	Void fraction
f	Frequency of pressure fluctuation [Hz]	β_t	Blade angle at the tip [degree]
k	Arbitrary integer	ϕ	Flow coefficient = v_1/U_t
m	Order number in θ	ϕ_d	Design flow coefficient =0.078
n	Order number in t	η	Hydraulic efficiency = P_o/P_i
N	Frequency of impeller rotation [Hz]	θ	Circumferential location relative to "stator" [degree]
N_v	Number of backflow vortices	θ^*	Absolute circumferential location [degree] ($\theta^* = \theta + \Omega_v t$)
p_1	Pressure at the inlet [Pa]		
p_2	Pressure at the outlet [Pa]	ρ	Density of water [kg/m^3]
p_a, p_b	Inlet fluctuating pressure [Pa]	σ	Cavitation number =$(p_1\text{-}p_v)/(\rho U_t^2/2)$
P_i	Input power [W]	ω	Angular frequency of rotating mode
P_o	Output power [W]	Ω	Relative angular velocity of rotor = $\Omega_n - \Omega_v$
p_v	Vapor pressure [Pa]	Ω_n	Angular velocity of rotor =$2\pi N$
r	Radial location [m]	Ω_v	Angular velocity of backflow vortices
R	Number of rotor blades	ψ_c	Local pressure coefficient =$(p\text{-}p_v)/(\rho U_t^2/2)$

R_t	Radius of inducer [m]
S	Number of stator blades
t	Time [s]
U_t	Tip speed [m/s]
v_1	Mean axial velocity at the inlet (z/D_t=0) [m/s]
v_z	Axial velocity [m/s]
v_θ	Absolute circumferential velocity [m/s]
z	Axial location measured from the leading edge at root [m]
ψ_s	Pressure rise coefficient =$(p_2-p_1)/(\rho U_t^2)$
$\Delta\psi$	Normalized amplitude of pressure fluctuation =$\Delta p_b /(\rho U_t^2)$

References

[1] Tsujimoto, Y., Horiguchi, H., Fujii, A., 2004, "Non-Standard Cavitation Instabilities in Inducers," Proceedings of the 10th International Symposium on Transport Phenomenon and Dynamic of Rotating Machinery, ISROMAC10-2004-020, pp. 1-11.

[2] Tsujimoto, Y., Yoshida, Y., Maekawa, M., Watanabe, S., and Hashimoto, T., 1997, "Observations of Oscillating Cavitations of an Inducer," ASME Journal of Fluids Engineering, Vol. 119, No. 4, pp. 775-781.

[3] Brennen,C., and Acosta, A.H., 1976, "The Dynamic Transfer Function for a Cavitating Inducer," ASME Journal of Fluids Engineering, pp. 182-191

[4] Tsujimoto, Y., Kamijo, K., and Yoshida, Y., 1993, "A Theoretical Analysis of Rotating Cavitation in Inducer," ASME Journal of Fluids Engineering, pp. 135-141.

[5] Watanabe, S., Sato, K., Tsujimoto, T., and Kamijo, K., 1999, "Analysis of Rotating Cavitation in a Finite Pitch Cascade Using a Closed Cavity Mode and a Singularity Method," ASME Journal of Fluids Engineering, Vol. 121, No. 4, pp. 834-840.

[6] Horiguchi, H., Watanabe, S., and Tsujimoto, Y., 2000, "A Linear Stability Analysis of Cavitation in a Finite Blade Count Impeller," ASME Journal of Fluids Engineering, Vol. 122, No. 4, pp. 798-805.

[7] Kamijo, K., Yoshida, M., Tsujimoto, Y., 1993, "Hydraulic and Mechanical Performance of LE-7 LOX Pump Inducer," Journal of Propulsion and Power, Vol. 9, No. 6, pp. 819-826.

[8] Kim, J.H., Atono, T., Ishizaka, K.,Watanabe, S., and Furukawa, A., 2008, "Rotating Behavior Observation of Cavitation in Inducer with Suction Axi-Asymmetrical Plate," Journal of Fluid Science and Technology, Vol. 3, pp. 744-753.

[9] Shimiya, N., Fujii, A., Horiguchi, H., Uchiumi, M., Kurokawa, J., and Tsujimoto, Y., 2008, "Suppression of Cavitation Instabilities in an Inducer by J-Groove," ASME Journal of Fluids Engineering, Vol. 130, No. 1, pp. 021302-1-021302-7.

[10] Kang, D., Yonezawa, C., Horiguchi, H., Kawata, Y., and Tsujimoto, Y., 2009, "Cause of Cavitation Instabilities in Three-Dimensional Inducer," International Journal of Fluid Machinery and Systems, Vol. 2, No. 3, pp. 206-214.

[11] Kang, D., Yonezawa, K., Horiguchi, H., Kawata, Y., and Tsujimoto, Y., 2009, "Inducer Design to Avoid Cavitation Instabilities," International Journal of Fluid Machinery and Systems, Vol. 2, No. 4, pp. 439-448.

[12] Hah, C., Mueller, M., Schiffer, H., 2008, "Aerodynamic Study of Circumferential Grooves in a Transonic Axial Compressor," ASME Fluid Engineering Conference, 55232, pp. 1-8.

[13] Frank, T., Lifante, C., Jebauer, S., Kuntz, M., and Rieck, K., 2007, "CFD simulation of Cloud and Tip vortex Cavitation on Hydrofoils," ICMF 2007, Leipzig, Germany, July 9-13, 2007, pp. 1-13

[14] Watanabe, T., Kang, D., Cervone, A., Kawata, Y., and Tsujimoto, Y., 2008, "Choked Surge in a Cavitating Turbopump Inducer," International Journal of Fluid Machinery and Systems, Vol. 1, No. 1, pp. 64-75.

[15] Tsujimoto, Y., Semenov, Y., 2002, "New Types of Cavitation Instabilities in Inducers," 4th International Conference on Launcher Technology "Space Launcher Liquid Propulsion", 2002, pp. 1-10.

[16] Subbaraman, M., Patton, M., 2006, "Suppressing Higher Order Cavitation Phenomena in Axial Inducers," Sixth International Symposium on Cavitation CAV2006, pp. 1-13.

[17] Yokota, K., Kurahara, K., Kataoka, D., Tsujimoto, Y., 1998, "A study of Swirling Backflow and Vortex Structure in the Inlet of an Inducer," Journal of the Japan Society of Mechanical Engineers, 64-622, pp. 51-58.

[18] Tyler, J.M., Sofrin, T.G., 1962, "Axial Compressor Noise Studies," SAE Transactions, 70, pp. 309-332.